EUROPHYSICS LETTERS 1 September 2006

Europhys. Lett., **75** (5), pp. 825–831 (2006)
DOI: 10.1209/epl/i2006-10174-9

Erosion waves: Transverse instabilities and fingering

F. Malloggi, J. Lanuza, B. Andreotti and E. Clément(*)
Laboratoire de Physique et Mécanique des Milieux Hétérogènes, UMR CNRS 7636 Univ. P6&P7 - 10, rue Vauquelin, 75005 Paris, France

received 6 March 2006; accepted in final form 13 July 2006
published online 28 July 2006

PACS. 83.50.Lh – Slip boundary effects (interfacial and free surface flows).
PACS. 92.40.Gc – Erosion and sedimentation; sediment transport.
PACS. 83.80.Fg – Granular solids.

Abstract. – Two laboratory scale experiments of dry and underwater avalanches of non-cohesive granular materials are investigated. We trigger solitary waves and study the conditions under which the front is transversally stable. We show the existence of a linear instability followed by a coarsening dynamics and finally the onset of a fingering pattern. Due to the different operating conditions, both experiments strongly differ by the spatial and time scales involved. Nevertheless, the quantitative agreement between the stability diagram, the wavelengths selected and the avalanche morphology suggest a common scenario for an erosion/deposition process.

Introduction. – Avalanching processes leading to catastrophic transport of various natural materials do not only occur in the air as we know of snow avalanches, mud flows and their catastrophic human and economical toll. Such events frequently happen below the sea level as they take many forms from turbidity currents to thick sediment waves sliding down the continental shelf. This is a fundamental feature shaping the submarine morphology. From the modeling of risks point of view, important questions still remain such as to evaluate to which extent an initial triggering event (an earthquake, an eruption, ...) would be responsible for a subsequent process that might propagate or amplify over large distances as an unstable matter wave. Unfortunately, the dynamics of such catastrophic events remains an issue so far lacking in conceptual clarity [1,2] since i) the rheology of the flows involved in an avalanche is complex and still not unravelled, ii) the physics of erosion/deposition mechanisms is essentially limited to empirical descriptions based on dimensional analysis and semi-empirical formulations. Recently, extensive laboratory scale experiments on dry granular materials have aimed to unify the rheology of dense particulate flows in different geometries [3]. These flows can be organized into two sub-classes, quasi-static creep flows characterised by an exponential-like velocity profile, and dense inertial flows, whose rheology is local [4–6]. In the case of fully developed granular flows, measurements are now sufficiently precise and reproducible to evidence dependencies of the constitutive relation on microscopic granular features like rough sandy material *vs.* round spherical particles [7,8]. But still, a full understanding of the flow constitutive relations would require a pertinent description of the passage between the blocked and the mobile

(*) E-mail: erc@ccr.jussieu.fr

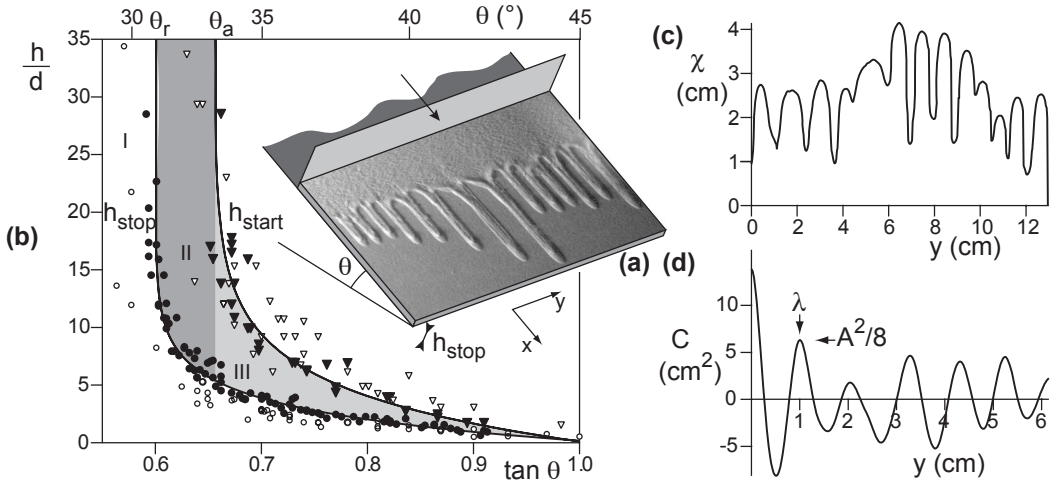

Fig. 1 – (a) Experimental set-up. (b) Stability diagram: $h_{\rm stop}$ is the thickness of the sediment left after an avalanche for a given angle θ, in air (●) and in water (○); $h_{\rm start}(\theta)$ is the maximum stable height of sediment, in air (▼) and in water (▽). $h_{\rm start}(\theta)$ and $h_{\rm stop}(\theta)$ are fitted by the form $h = b\ln((\tan\theta - \mu)/\delta\mu)$ where $b = -2.7d$, $\mu = 0.6$ for $h_{\rm stop}$ ($\mu = 0.65$ for $h_{\rm start}$) and $\delta\mu = 0.43$ are fitting parameters (solid lines). In region I, an avalanche front cannot propagate autonomously down the slope: the perturbation is bound to fade away when the driving stops. Avalanches triggered in region II are stable while they exhibit a transverse instability in region III. In particular, solitary erosion waves are evidenced when starting from the stable height $h_{\rm stop}$. (c) Front profile $\chi(y)$ obtained after image processing by a correlation technique. (d) The corresponding correlation function $C(y)$ allows to define the average wavelength λ and amplitude A.

phases (the jamming transition). For instance, the onset and the dynamics of triangular-shape avalanches was shown to be controlled essentially by the presence of a metastable substrate and the interplay between erosion and deposition processes [9, 10]. From a theoretical point of view, descriptions of the granular bed mobilisation have been proposed, either empirically ("*à la* Saint-Venant") [11, 12] or phenomenologically by phase field methods [13]. Avalanche fronts flowing on solid rough substrates are transversally stable, the transverse coupling due to gravity being essentially a stabilizing mechanism [14, 15]. But, as soon as segregation occurs, for instance in the bi-disperse case, an avalanche front may exhibit a fingering pattern explained by a pinning mechanism [16, 17]: the grains of larger size gathering in the finger thrusts are hindering locally the avalanche front progression. In this paper, we present an experimental study of avalanche fronts developing over an erodible granular substrate, in the air and underwater. We demonstrate the existence of a linear transverse instability of solitary erosion waves, although the rough grains we use exhibit a narrow polydispersity (25%).

Experiment. – The avalanching set-ups consist of a thin layer of grains deposited on a substrate that can be tilted at a value θ (fig. 1a). The dry granular set-up is similar to the one of Daerr *et al.* [9, 10]. The avalanche track is 70 cm wide and 120 cm long. The granular medium is Fontainebleau sand of a medium size $d = 300 \pm 60\,\mu$m and the track bottom is made of black velvet. For underwater avalanches, the set-up size is quite smaller. The avalanche track is the bottom of a plexiglass tank that can be tilted up to an angle θ from a horizontal position. The avalanche track width is 15 cm and so is the track length. The granular sediment is an aluminum oxide powder of size either $d = 30\,\mu$m or $40 \pm 11\,\mu$m. To avoid interparticle co-

hesion, it is sufficient to maintain the *p*H value close to 4 by adequate addition of hydrochloric acid [18]. The substrate is initially set at a horizontal position and a fixed mass of powder is poured and suspended by vigorous stirring. A uniform sediment layer of height h then forms within 10 min. The bottom is an abraded but transparent plexiglass plate which offers the possibility to monitor the avalanche dynamics by transparency when illuminated from below. The profile of the avalanche front $h(x,t)$ is obtained with a laser slicing technique and is resolved within 30 μm ($0.1d$) in the dry case. The front dynamics is quantitatively monitored by image processing of the avalanche front pictures. The front line equation $\chi(y,t)$ is then extracted (fig. 1c) and the front line auto correlation function $C(y,t) = \langle \chi(y+y',t)\chi(y',t)\rangle_{y'}$ is computed. Then, the correlation function first maximum is identified from which we define the average wavelength λ and the amplitude $A = 2\sqrt{2C(\lambda)}$ (fig. 1d). In addition, for dry avalanches, we measure the surface velocity field using a Particle Image Velocimetry technique.

Results. – It has been shown that the stability of dry granular layers of depth h lying on a substrate inclined at an angle θ can be simply apprehended by a diagram with two branches [14] (fig. 1b), $h_{\rm start}(\theta)$ and $h_{\rm stop}(\theta)$, with the following interpretation: a uniform deposit of height h will globally loose stability if tilted above the angle θ defined by $h = h_{\rm start}(\theta)$ and the avalanching process will leave at rest a deposit of height $h_{\rm stop}(\theta)$. The $h_{\rm start}(\theta)$ and $h_{\rm stop}(\theta)$ curves diverge at an asymptotic angle limit, respectively equal to the avalanche angle of the granular pile θ_a and to the repose angle θ_r. Between the two, a domain of metastability for the granular deposit is present. Interestingly, the stability curves obtained for dry (sand-velvet) and underwater (alumina-rough plexiglass) layers bear the same features and fall apparently on the same curve when the deposited height is rescaled by d (fig. 1b).

To initiate avalanche fronts both in air and underwater, we designed a "bulldozer" technique where a plate perpendicular to the avalanche track scrapes the sediment at a constant velocity (fig. 1a). Although our results on avalanche stability are valid in the whole metastable region (fig. 1b), we will limit ourselves here to experiments started from a stable sediment layer of height $h_{\rm stop}(\theta)$. Once an autonomous avalanche front separates from the plate, the bulldozer driving stops. For $\theta_r < \theta < \theta_a$, we always obtain transversely stable autonomous avalanche fronts, both in the wet and dry cases. We observed that the avalanche quickly converges toward a "shark tooth" form which then remains constant. It reminds the shape of solitary waves found for viscous liquids falling down an incline [19,20]. Here, the solitary wave is found to be quite insensitive of the range of scraping velocities but depends on the mass set into motion. For this systematic study, we have kept a constant scraping velocity at about one-third of the typical avalanche velocity v_a and put the minimal mass required to trigger a solitary wave. In these conditions, for each value of the —unique— control parameter θ, there is thus a single possible solitary erosion wave. In water, v_a is of the order of the Stokes velocity $\dfrac{\Delta\rho}{\rho_w}\dfrac{gd^2}{18\nu} \simeq 2\,\mathrm{mm/s}$, where $\dfrac{\Delta\rho}{\rho_w} = 3$ is the density contrast between grains and water, ν the water kinematic viscosity and g the gravity acceleration. In the air, the propagation velocity is of the order of $\sqrt{gd} \simeq 5\,\mathrm{cm/s}$. Figure 2(a) shows a spatio-temporal diagram obtained by extracting subsequent vertical pixel lines and adding them together horizontally to build the time base. We observe simultaneously the deviation of the laser spot corresponding to the time-resolved height. In fig. 2(b), the local sediment height h and local surface velocity v profiles are extracted for the same avalanche. The space and time origins are shifted to match the front onset. Independently, we measured the flow rule on homogeneous steady flows and found $v/\sqrt{gh} = \beta(h/h_{\rm stop} - 1)$, with $\beta = 0.8$, as previously found for sand [3]. Here, this equilibrium relation remains verified in the tail of the avalanche. Furthermore, we directly observe the presence of a thin layer of grains flowing on a jammed substrate before stopping.

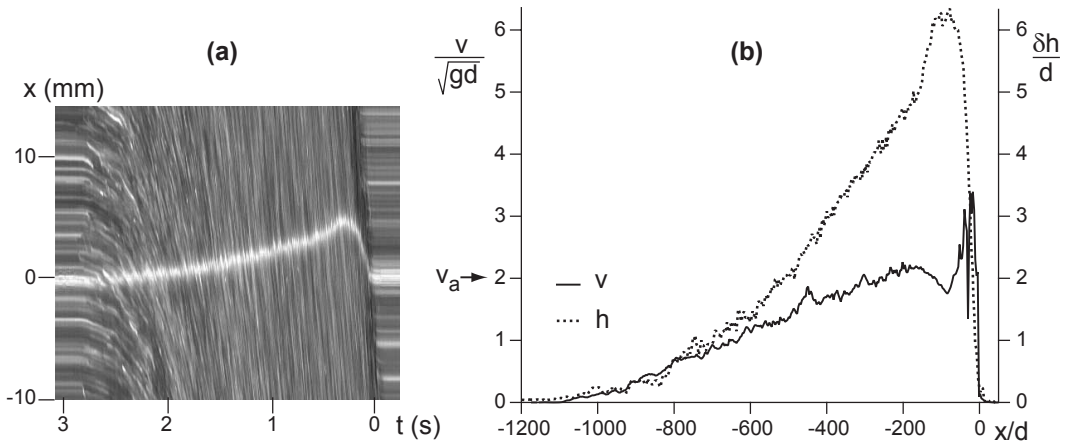

Fig. 2 – (a) Spatio-temporal diagram done with a fast camera (125 Hz), showing the particle motion (the slope of the streaks is the velocity) as well as the profile height (deflection of the laser sheet). (b) Solitary erosion-wave profile $\delta h = h - h_{\mathrm{stop}}$ (in the air) rescaled by d (dotted line) and surface velocity profile v rescaled by $\sqrt{gd}$ (solid line) (dry, $\theta = 32^\circ$, $h_{\mathrm{stop}} = 2.3\,\mathrm{mm} = 7.8d$, region II). It can be observed that the surface grain velocity tends at the front towards the solitary-wave velocity v_a.

The important issue of the existence of a static layer below the flowing one will be adressed in a forthcoming paper. For $\theta > \theta_a$ the neutral wavefronts are transversally unstable (fig. 3). It is worth noticing that for the same angles, avalanches down a solid rough plate are stable (at least in the dry case). After the initial instability, we have identified a sequence of fusion processes increasing the spatial modulation lengths (coarsening scenario). Finally, the transverse destabilization ends up as a fingering pattern. In this final stage, the flowing zones are disconnected one from the others so that the wavelength does not evolve anymore.

In fig. 4, we display a typical time evolution of the dominant wavelength extracted from the correlation function. In the inset, a typical fusion event is displayed to illustrate the coarsening scenario. Because of the competition between unstable modes and the coarsening process taking place, the identification of a generic scenario for the transverse instability is problematic. This is the reason why, in addition to the experiments started from a flat bed

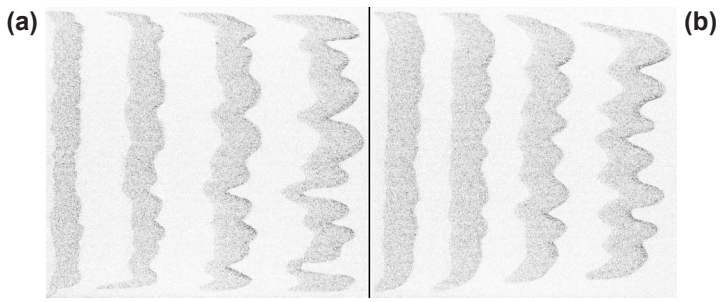

Fig. 3 – Region III. Flowing part of solitary waves visualised by image difference (air, $d = 300\,\mu$m, $\theta = 35^\circ$, time interval 1.1 s), starting from a flat bed (a) or from an initial bed presenting a forced wavelength $\lambda = 6.5\,$cm (b).

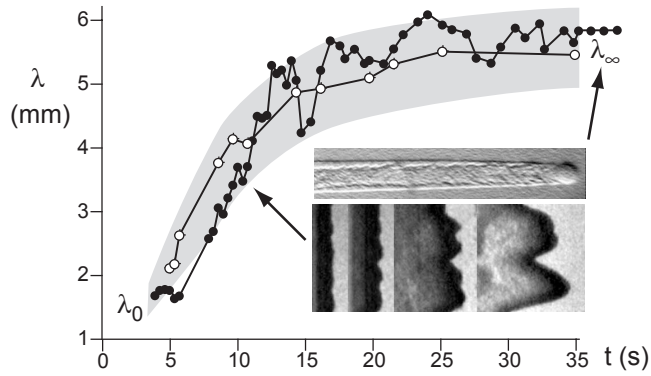

Fig. 4 – Time evolution of the wavelength λ (water, $d = 40\,\mu$m, $\theta = 37.1^\circ$) in a single typical realisation (●) and averaged over realisations (solid line) —the shadow zone indicates the standard deviation. After a small plateau at the initial wavelength λ_0, λ increases due to merging processes (lower photograph) until the value λ_∞ which corresponds to the formation of non-interacting fingers (upper photograph).

we just described, we performed series of experiments starting from a modulated initial condition (fig. 3). The modulation at a given wavelength is simply produced by imprinting on the sediment surface regularly spaced thin scarifications (shallow scratches). We find that the forced modes always fade away in region II, but on the other hand, in region III, the front modulations amplifies exponentially for a wide band of modes. The linear regime is clearly evidenced over one decade in amplitude (see fig. 5(a)). Non-linear effects start being visible when the amplitude becomes centimetric. Figure 5(b) shows the dispersion relationship deduced from these experiments, which demonstrates the existence of an initial long-wavelength linear instability. The parabolic fit is consistent with the theoretical prediction of [21].

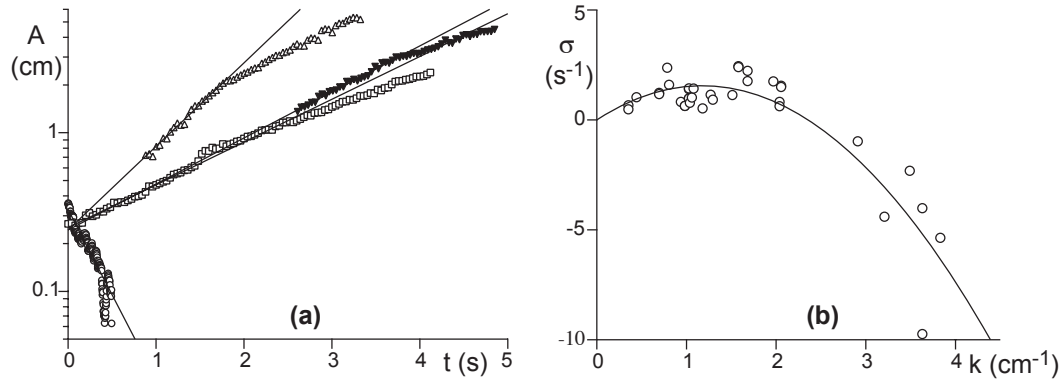

Fig. 5 – (a) Time evolution of the amplitude (air, $d = 300\,\mu$m, $\theta = 35^\circ$) when the initial condition is forced at a given wavelength $\lambda = 12$ mm (○), $\lambda = 30$ mm (□), $\lambda = 90$ mm (△) and $\lambda = 178$ mm (▼). (b) Linear growth rate σ as a function of the wave number k. The solid line is the best fit by $\sigma = a|k| - bk^2$, with a maximum growth rate of $2.5\,\mathrm{s}^{-1}$ attained at $\lambda_0 \simeq 4$ cm. Measurement of λ_0 from an undisturbed solitary wave (fig. 3) gives 3.3 cm.

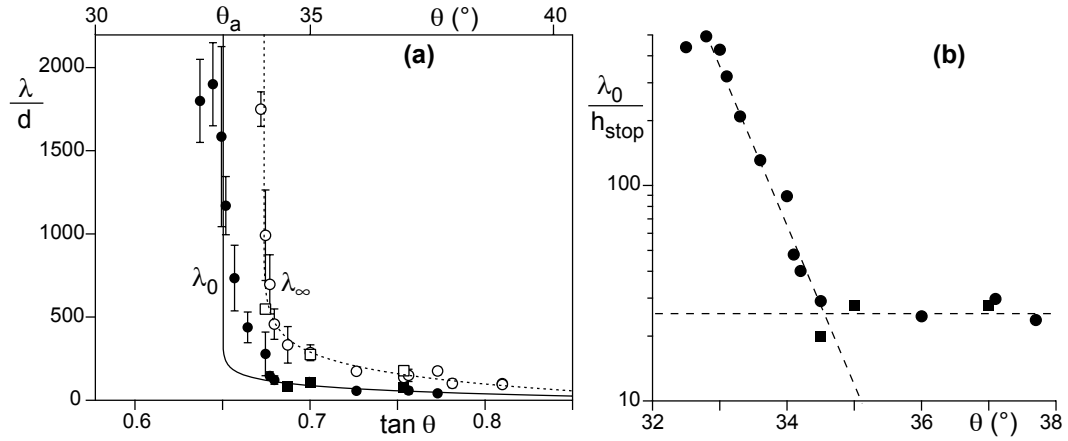

Fig. 6 – (a) Initial (●) and final (○) wavelengths rescaled by d as a function of θ ($d = 40\,\mu$m, in water). The initial wavelength data in air (■) and water (●) coincide, as well as the final wavelength data in air (□) and water (○). The error bars correspond to the dispersion of the data from a realisation to the other. As λ_0 diverges at θ_a, we have superimposed the curve $10h_{\rm start}(\theta)$ (solid line), which is a good approximation of λ_0 to the first order. The dotted line is the best fit of the final wavelength λ_∞ by the same logarithmic form as $h_{\rm start}(\theta)$ or $h_{\rm stop}(\theta)$. (b) Initial wavelength λ_0 rescaled by $h_{\rm stop}(\theta)$, as a function of the plane angle θ.

For experiments both in the air and underwater performed in the unstable regime, we extract the two characteristic wavelengths. The initial wavelength λ_0 would correspond, to the best of our experimental possibilities, to the fastest growing mode of the linear regime. Then, the wavelength λ_∞ is taken at the onset of the fingering instability. In fig. 6, we display both wavelengths rescaled by the grains sizes: λ_0/d and λ_∞/d, as a function of the inclination angle θ. The selected wavelengths are typically larger than a grain size by at least two orders of magnitude. Note that the largest wavelengths measured are of the order of the track width ($1800d$ in water and $750d$ in air). Furthermore, in the limit of finite-size effects and measurements uncertainties, we find that a value $\theta \cong \theta_a$ corresponds to a diverging boundary for the initial wavelength λ_0/d. Hence this is a signature of a zero wave number instability with a threshold close to θ_a. In fig. 6b, this divergent lengthscale is rescaled by $h_{\rm stop}(\theta)$ which turned out to be the correct characteristic length scale for the flow rheology. Although the wavelength seems to scale on $h_{\rm stop}$ at large angle, one can observe a growth at least exponential close to the threshold. Let us emphasize that data obtained in the air and underwater collapse *on the same curve*, once rescaled by the grain size (or $h_{\rm stop}$). In the range of parameters where the fingering regime is reached before the end of the track, the ratio of the final to the initial wavelength is approximately constant and equal to $\lambda_\infty/\lambda_0 \simeq 3.5$. The presence of a fingering instability is a quite fascinating feature of this avalanching process. Here, the fingering front stems from the onset of localized propagating waves following the transverse instability regime. These fingers are localized matter droplets with levees on the side and propagating in a quasi-solitary mode and when they are fully developed, their selected width is found to be quite sensitive to the slope ($\simeq \lambda_0$ for both wet and dry cases).

Conclusion. – In this letter, we have investigated the dynamics of underwater and dry granular avalanches taking place on an erodible substrate. We have identified the domain of existence for solitary waves going down the slope without changing form. For angles larger

than the avalanche angle, we proved the existence of a linear transverse instability which further develops via a coarsening fusion process and finally ends up as a fingering pattern. The scenario is a standard zero wave number instability of threshold close to θ_a. The existence of solitary waves provides a new important test to models. For instance, it will be interesting to determine their existence in Saint-Venant models that include or not a static erodible layer below the avalanche. The mechanism responsible for the instability remains yet to be found but it is clearly related to a flux of matter from the slower towards the faster moving parts of the front. Different effects can be invoked like a gravity effect if the local slope strongly decreases in the foremost zones, or an anisotropy of normal stresses leading to a reduced "pressure" in the fluidized zones. A recent study based on the partial fluidization model [13] has recovered the existence of solitary waves and the fingering instability [21], here related to a reduced friction in the flowing zones. Further studies with other materials on different substrates are needed to determine to which extent the instability is generic. A further challenging experimental issue is to get a more focused vision on the interface separating the jammed and the rolling phases, and its relation to the instability onset. In the final stage of the instability, fingers appear as droplet-like solutions of the erosion/deposition process and thus look essentially different from the segregation fingers reported on a rough substrate [16]. Note that their shape is reminiscent of many natural patterns obtained in debris or mud flows [17] which also display surprinsigly well-selected widths at values about hundreds of a typical rock size.

* * *

We thank P. Claudin, O. Pouliquen, A. Daerr and I. Aranson for many discussions and suggestions on the experiment.

REFERENCES

[1] Iverson R. M., *Rev. Geophys.*, **35** (1997) 245296.
[2] Hampton M. A., Lee H. J. and Locat J., *Rev. Geophys.*, **34** (1996) 3359.
[3] Midi G. D. R., *Eur. Phys. J. E*, **14** (2004) 341.
[4] da Cruz F., Emam S., Prochnow M., Roux J-N. and Chevoir F., *Phys. Rev. E*, **72** (2005) 021309.
[5] Ertaş D. and Halsey T. C., *Europhys. Lett.*, **60** (2002) 931.
[6] Pouliquen O., *Phys. Rev. Lett.*, **93** (2004) 248001.
[7] Forterre Y. and Pouliquen O., *J. Fluid Mech.*, **486** (2003) 21.
[8] Borzsonyi T., Halsey T. C. and Ecke R. E., *Phys. Rev. Lett.*, **94** (2005) 208001.
[9] Daerr A. and Douady S., *Nature*, **399** (1999) 241.
[10] Daerr A., *Phys. Fluids*, **143** (2001) 2115.
[11] Bouchaud J., Cates M., Prakash J. and Edwards S., *J. Phys. I*, **4** (1994) 1383.
[12] Douady S., Andreotti B. and Daerr D., *Eur. Phys. J. B*, **11** (1999) 131.
[13] Volfson D., Tsimring L. S. and Aranson I. S., *Phys. Rev. E*, **68** (2003) 021301.
[14] Pouliquen O., *Phys. Fluids*, **11** (1999) 542; 1956.
[15] Pouliquen O. and Valance J. W., *Chaos*, **9** (1999) 621.
[16] Pouliquen O., Delour J. and Savage S. B., *Nature*, **386** (1997) 816.
[17] Felix G. and Thomas N., *Earth Planet. Sci. Lett.*, **221** (2004) 197.
[18] Daerr A., Lee P., Lanuza J. and Clément E., *Phys. Rev. E*, **67** (2003) 065201.
[19] Kapitza P. L. and Kapitza S. P., *Zh. Eksp. Teor. Fiz.*, **19** (1949) 105.
[20] Pumir A., Manneville P. and Pomeau Y., *J. Fluid Mech.*, **135** (1983) 27.
[21] Aronson I. S., Malloggi F. and Clément E., *Phys. Rev. E*, **7** (2006) 050302(R).